Journal of Alloys and Compounds 510 (2012) 107–113

Contents lists available at SciVerse ScienceDirect

Journal of Alloys and Compounds

journal homepage: www.elsevier.com/locate/jallcom

# Structural properties of $Zr_xCu_{90-x}Al_{10}$ metallic glasses investigated by molecular dynamics simulations

C.C. Wang, C.H. Wong*

*School of Mechanical & Aerospace Engineering, Nanyang Technological University, 50 Nanyang Avenue 639798, Singapore*

ARTICLE INFO

*Article history:*
Received 18 April 2011
Received in revised form 25 July 2011
Accepted 30 July 2011
Available online 7 September 2011

*Keywords:*
MD simulations
Zr–Cu–Al metallic glasses
Common neighbor analysis
Atomic-level structure

ABSTRACT

In this work, we employed classical molecular dynamics simulations to study $Zr_xCu_{90-x}Al_{10}$ metallic glasses with a wide metallic compositions ranging from 20% to 70%. Radial distribution functions were used to determine interactions between like and unlike bonds and the corresponding interatomic distances. The results showed evidence of short-range order (SRO) in Cu–Al and Al–Zr pairs. The average interatomic distance of the Cu–Al bond was observed to be shortened by 6% in all the systems studied. Analysis of coordination numbers (CNs) indicated that the total CN is nearly invariant in these systems. Finally, common neighbor analysis was conducted to determine icosahedral ordering. The result revealed that the addition of a low Al concentration to Zr–Cu alloys exhibits more prominent icosahedral ordering, except at the Zr-rich end.

## 1. Introduction

The first preparation of metallic glass (MG) occurred in 1960 [1]. Since then, many studies of their structures have been conducted at the atomic level in order to reveal the fundamental root of their superior mechanical properties and resistance to wear and corrosion [2–4]. Currently, it is widely accepted that short- to medium-range order exists in MGs, which are packed in quasi-icosahedral clusters [3].

Recently, there has been a huge interest in the atomic-level structure and structure–property relationship in MGs [5]. Of particular interest is the binary Zr–Cu system, which is widely regarded as a good candidate for bulk metallic glasses (BMGs). As such, there have been extensive efforts to investigate Zr–Cu systems both experimentally and theoretically. For example, using the Zr–Cu binary system, Li et al. showed that there is a clear correlation between density change and glass-forming ability [6]. Mattern et al. studied the structural and thermal stability of rapidly quenched amorphous Zr–Cu alloys in a wide compositional range [7,8] via high-energy X-ray diffraction, atomic pair correlation functions, and calorimetric data. The results exhibited monotonic changes with composition. The same team also investigated the structural behavior of $Zr_{50}Cu_{50}$ and $Zr_{35}Cu_{65}$ MGs under uniaxial tensile stress by high-energy X-ray synchroton diffraction [9]. They found that anelastic deformations are accompanied by bond reorientation, which leads to direction-dependent changes in the chemical SRO. The local atomic structure of Zr–Cu amorphous alloys was also studied by the extended X-ray adsorption fine structure method (EXAFS) [10]. It was found that icosahedral symmetry dominates in the local atomic structure of these systems. The authors also concluded that the addition of Al as an alloying element results in considerable deviation from the random mixing behavior observed in binary Zr–Cu alloys.

Numerous theoretical studies have also been conducted on Zr–Cu systems. Sha et al. [11] employed atomistic methods for studying Zr–Cu MGs and discovered that the changes in Cu-centered full icosahedra are the fundamental structural factors that determine the ease of glass formation. They also found that in Zr–Cu MGs, an icosahedral shell structure prevails in both short and medium ranges [12]. Almyras et al. investigated the microstructure of $Zr_{35}Cu_{65}$ and $Zr_{65}Cu_{35}$ MGs and found that these systems consist of small touching and/or interpenetrating icosahedral-like clusters. These clusters obey a simple rule that takes into account the system's stoichiometry [13]. They concluded that this approach allows the prediction of the MG microstructure, which could then be used for experimental data interpretation and the design of new MGs. Zhang et al. employed molecular dynamics (MD) simulations for studying structural anisotropy in $Zr_{50}Cu_{50}$ and $Zr_{35.5}Cu_{64.5}$ MGs, which is induced by static uniaxial loading within the elastic regime [14]. They found that the degree of anisotropy within the elastic regime increases with the applied load, following an exponential growth function. Kang et al. investigated the correlation between experimentally observed plasticity and various properties of Zu–Cr BMG materials using atomistic simulations [15]. It was reported

---

* Corresponding author. Tel.: +65 67905913.
*E-mail address:* chwong@ntu.edu.sg (C.H. Wong).

0925-8388/$ – see front matter © 2011 Elsevier B.V. All rights reserved.
doi:10.1016/j.jallcom.2011.07.110

that most of the examined properties show a composition dependency that is roughly comparable to the experimentally observed plasticity for Zr–Cu BMG alloys.

In addition to binary Zr–Cu systems, ternary Zr–Cu–Al systems have also been widely researched because of their significantly lower critical cooling rate for glass formation and improved strength [16,17]. For example, the relationships among the cooling rate, Al content, microstructure, and mechanical properties were established through a systematic investigation of primary phase precipitation in $(Zr_{0.5}Cu_{0.5})_{100-x}Al_x$ alloys [18]. It was found that the formation of metastable austenitic Zr–Cu phases can be improved by the addition of Al, and composite structures with B2–Zr–Cu particles can be formed in alloys containing 3–8% Al. A recent study by Yu et al. reported that the mechanical properties of $Zr_{46}Cu_{46}A_{l8}$ BMGs after quasi-static compression are related to the changes in free volume, density, and structure [19]. Cui et al. conducted MD simulations on Zr–Cu–Al systems and revealed that the physical origin of MG formation is the collapse of the crystalline lattice while solute atoms exceed the critical value, resulting in a hexagonal composition region within which the Zr–Cu–Al ternary MG formation is energetically favored [20]. Ishii et al. investigated the relaxation and crystallization behaviors of $Zr_{50}Cu_{40}Al_{10}$ BMGs using EXAFS [21] and found that the ternary BMG has a chemical order around the free volume.

Moreover, numerous studies have been performed to determine the reasons behind the differences in the properties of binary Zr–Cu and ternary Zr–Cu–Al systems. For example, Cheng et al. performed classical MD simulations on $Zr_{47}Cu_{46}Al_7$ MGs to study the effect of Al content [22]. The authors found that a small percentage of Al in the ternary MG has a stabilizing topological effect, and that electronic interactions involving Al are both bond specific and environment specific [22]. In addition, both experimental and computational methods have been employed to investigate the amorphous $Zr_{46}Cu_{46}Al_8$ alloy [23]. It was found that Al atoms distribute homogeneously around Cu and Zr atoms without segregation and the addition of Al increases the amount of icosahedron-like clusters and contributes to a more homogeneous distribution among different polyhedra.

However, these reported studies mainly focus on a single representative system of Zr–Cu–Al MGs. To date, there has been no systematic investigation of a series of Zr–Cu–Al systems, and the structural dependence of the compositions of Zr and Cu elements remains unknown. In this paper, classical MD simulations with embedded-atom method (EAM) potentials were employed to study amorphous $Zr_xCu_{90-x}Al_{10}$ alloys ($x$ = 20, 30, 40, 50, 60, and 70). On the basis of these simulations, radial distribution functions (RDFs), CNs, and the distribution of Honeycutt–Andersen (H–A) indices [24,25] have been obtained. The results show that icosahedral ordering favors low to medium Zr concentrations.

## 2. Simulation details

### 2.1. Potential functions

It is well known that the accuracy of an atomistic simulation depends on the potential function. Many studies of MGs have adopted pairwise potentials such as the Lennard–Jones potential [26,27]. However, it has been reported that pairwise potentials are unable to accurately describe the properties of amorphous metals, which include the Cauchy discrepancy of elastic constants, vacancy formation energies, stacking fault energies, surface structure, and relaxation [28,29]. On the contrary, a many-body potential such as the EAM potential overcomes these inadequacies and is better able to reproduce some basic features of metallic systems.

In this study, we adopted the EAM potential to describe interatomic interactions in the simulation model. The potential consists of simple embedding energy functions and short-range pairwise potential functions, and is given by [29]

$$E_{tot} = \sum_i F_i(\rho_{h,i}) + \frac{1}{2} \sum_{\substack{i,j \\ i \neq j}} \phi_{ij}(R_{ij}) \tag{1}$$

where $\phi_{ij}$ is the short-range pair potential and $R_{ij}$ is the distance between atoms $i$ and $j$. The host density $\rho_{h,i}$ is approximated by the total atomic densities $\rho^a$, i.e., $\rho_{h,i} = \sum_{j(\neq i)} \rho_j^a(R_{ij})$. Here $\rho_j^a$ is the contribution to density from atom $j$. In essence, energy is, therefore, a simple function of the positions of atoms.

Therefore, in this study, there are six pairwise potential functions and three embedding functions for ternary Zr–Cu–Al alloys. The parameters for the pairwise and embedding functions are adapted from reference [22].

### 2.2. Computational model and analysis methods

The model used in the simulations is a series of $Zr_xCu_{90-x}Al_{10}$ alloys ($x$ = 20, 30, 40, 50, 60, and 70) with a total of 16,000 atoms randomly arranged in a body-centered cubic (bcc) supercell. The initial positions of Zr, Cu, and Al atoms were allocated according to their proportions. The initial temperature was set at 2100 K, which is far above the melting point of the ternary alloy. In the simulations, periodic boundary conditions were applied in all three axial directions. The MD timestep was set at 1 fs, which is small enough to prevent any discretization errors. The external pressure was set to zero to initialize the supercell over 500,000 timesteps under the isothermal isobaric (NPT) ensemble [30], where moles (N), pressure (P), and temperature (T) are conserved. As a result, we obtained a well-equilibrated liquid state.

The system was then allowed to cool down from 2100 K to 300 K. The cooling was performed in two steps. The Berendsen thermostat [31] was used to reduce the temperature by 25 K over 2000 timesteps and the system was then equilibrated under the NPT ensemble for another 500,000 timesteps. During the latter process, properties such as volume, potential energy, and enthalpy were recorded and averaged. After 72 iterations, the system temperature will eventually reach 300 K. Therefore, our cooling rate was calculated to be $5 \times 10^{10}$ K/s. After cooling, the system was kept in the NPT ensemble at 300 K for another $5 \times 10^7$ timesteps. The configurations and atom coordinates were saved at each equilibration stage and the final stage for further studies.

After obtaining the amorphous Zr–Cu–Al alloys in the simulations, the RDFs were employed to determine the correlation between the atoms. The partial radial distribution function (PRDF) can be expressed as [32]

$$g_{\alpha\beta}(r) = \frac{V}{N_\alpha N_\beta} \left\langle \sum_i^N \sum_{j \neq i}^N \delta(r - r_{ij}) \right\rangle \tag{2}$$

where $V$ is the volume of the system, $N_\alpha$ and $N_\beta$ are the number of atoms $\alpha$ and $\beta$, respectively, $r_{ij}$ represents the distance between atoms $i$ and $j$, $\delta(r–r_{ij})$ is the Dirac delta function, and the angular brackets represent the time average. The total RDF of atom $i$ is denoted by $g_i(r)$ and is the sum of the PRDFs for atom $i$ to atom $j$, written as $g_i(r) = \sum_j g_{ij}(r)$ Similarly, the total RDF for the system is computed as $g_{tot}(r) = \sum_i g_i(r)$.

To quantitatively determine the bonding preferences of different elements, the PRDF was integrated to generate the CNs. It can be calculated as

$$N_{ij} = \int_0^{r_{\min}} 4\pi r^2 \rho_j g_{ij}(r)\, dr \tag{3}$$

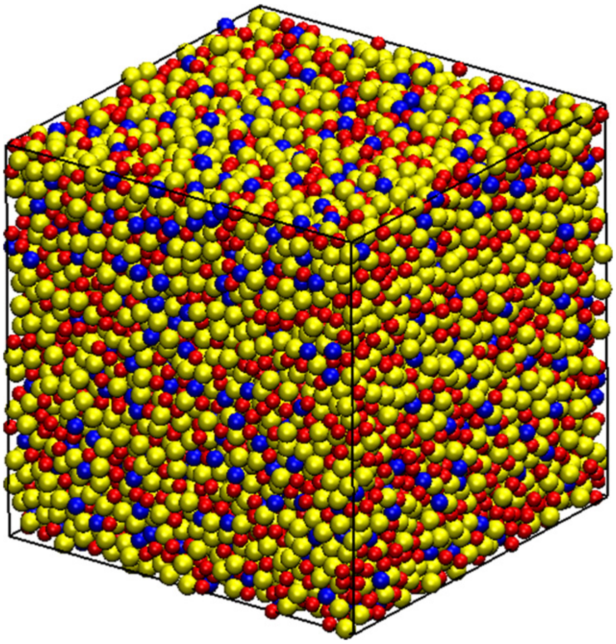

**Fig. 1.** Simulation model of $Zr_{50}Cu_{40}Al_{10}$ in final amorphous state. Yellow, red, and blue balls represent Zr, Cu, and Al atoms, respectively.

where atom *i* is the center atom, atom *j* is the neighbor atom, $r_{min}$ is the radial distance corresponding to the first minimum value of $g_{ij}(r)$, and $\rho_j$ is the atomic density of atom *j*. The total CN for atom *i* is calculated as $N_i = \sum_j N_{ij}$.

Finally, H–A indices were employed to analyze the icosahedral ordering present in these systems. Three indices were used to describe different H–A pairs. The first index is 1 if the root pairs are bonded and 2 if the root pairs are not bonded. The second index represents the number of common nearest-neighbor atoms shared by the root pairs, and the last index represents the number of bonds among neighbor atoms. In general, a bcc structure is characterized by 166-type and 144-type pairs, while face-centered cubic (fcc) and hexagonal close packed (hcp) structures are characterized by 142-type pairs [33]. In amorphous metals, a perfect icosahedron contains 12 fivefold 155-type pairs, while 154-type and 143-type pairs are regarded as compositions of a distorted icosahedron [34].

## 3. Results and discussion

### 3.1. Glass transition

In our simulations, all the six systems become glassy with the cooling rate of $5 \times 10^{10}$ K/s. An example of a glassy system is shown in Fig. 1, which depicts the final amorphous state of $Zr_{50}Cu_{40}Al_{10}$ with 8000 Zr atoms, 6400 Cu atoms, and 1600 Al atoms. It is well known that glass transitions are characterized by the absence of a discontinuity in volume (*V*) and enthalpy (*H*) as a function of temperature (*T*). However, when glass transition takes place near the glass transition temperature, the *V*/*T* and *H*/*T* gradients are smaller because of lower thermal expansion of solids. Fig. 2(a) illustrates how enthalpy changes with decreasing temperature of $Zr_xCu_{90-x}Al_{10}$ alloys. By dividing the curves into two lines, we obtain the glass transition temperature at the intersection point. In Fig. 2(b), we show that the glass transition temperature for $Zr_{50}Cu_{40}Al_{10}$ MG is around 680 K, which agrees well with the experimental data of 670–679 K reported by Nagai et al. [35]. The largest error between our calculated results and the experimental data is therefore around 1.5%.

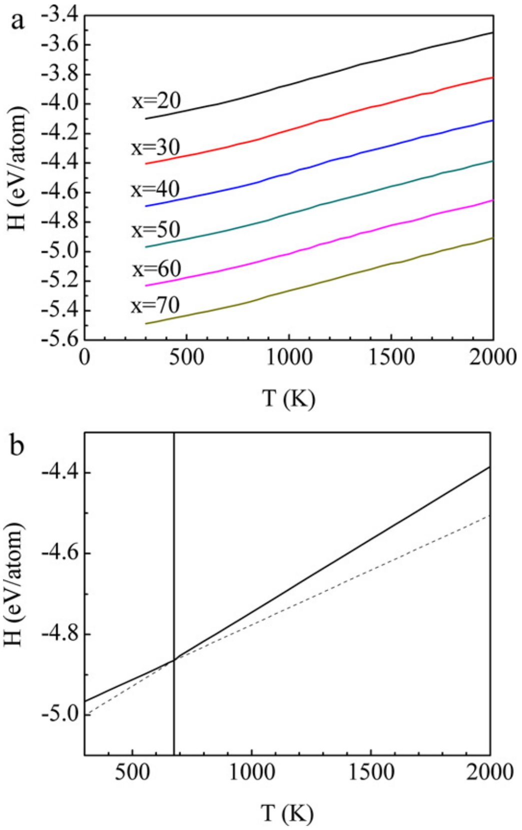

**Fig. 2.** Enthalpy as a function of temperature for (a) $Zr_xCu_{90-x}Al_{10}$ alloys and (b) $Zr_{50}Cu_{40}Al_{10}$ alloy. Dotted lines in (b) are extrapolated from the H–T curve. The vertical line indicates the glass transition temperature.

In addition, the dependence of atomic number density on composition is shown in Fig. 3. The number density increases with increasing Cu concentrations, and this is consistent with the experimental results for binary Zr–Cu alloys studied in reference [7]. This comparison is reasonable since in this study, the concentration of Al is kept low and constant at 10%.

### 3.2. Radial distribution functions (RDFs)

Fig. 4 shows the total RDFs for $Zr_xCu_{90-x}Al_{10}$ alloys at 300 K. The RDF of every system exhibits a distinct first peak indicating that there exists a strong SRO. We also observe that the first peak

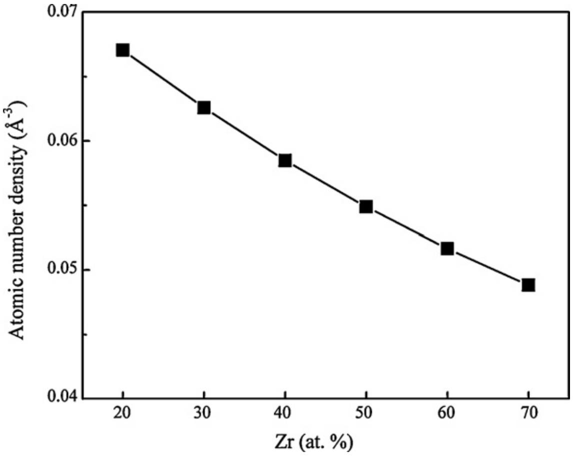

**Fig. 3.** Atomic number density for amorphous $Zr_xCu_{90-x}Al_{10}$ alloys.

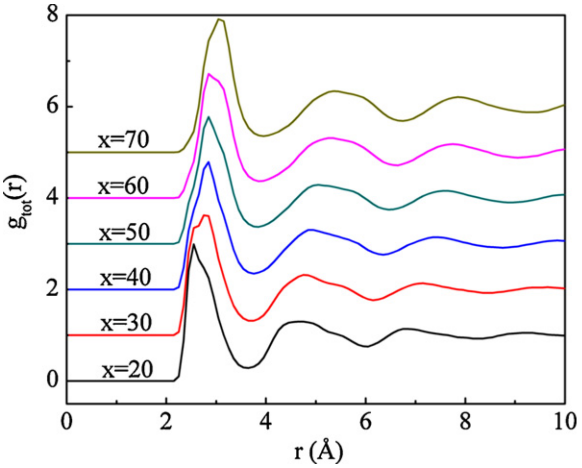

**Fig. 4.** Total RDFs for amorphous $Zr_xCu_{90-x}Al_{10}$ alloys. Individual curves corresponding to different alloys are displaced vertically for clarity.

shifts toward larger radial distance values with increasing Zr concentrations, since the radius of a Zr atom is larger than that of a Cu atom.

Figs. 5 and 6 show the PRDFs for like and unlike bonds in these systems, respectively. As illustrated in Fig. 5, like bonds exhibit strong sensitivity to atomic concentrations. For example, in Zr–Zr PRDFs, the first peak becomes higher when the concentration of Zr increases. On the contrary, the Cu–Cu pair shows a stronger SRO at the Cu-rich end. Unlike Zr–Zr and Cu–Cu pairs, the first peak of the Al–Al pair (Fig. 5(c)) is not as prominent because of the low concentration of Al atoms. Fig. 6, which depicts the PRDFs for unlike bonds, shows that atomic density is not significantly affected by the radial distance despite different atomic concentrations. Instead, intensive interactions among the three unlike pairs can be observed in all systems. For example, even though the ternary alloy consists of only 10% Al, there are strong Al interactions with Cu and Zr, as evidenced by the prominent first peaks seen in Cu–Al and Al–Zr PRDFs.

From the PRDFs, we extracted the interatomic distances and listed them in Table 1. Comparison of these values with Goldschmidt radii ($R_{Zr} = 1.6$ Å, $R_{Al} = 1.43$ Å, $R_{Cu} = 1.28$ Å) reveals that the only significant difference exists for the Cu–Al pair, in which the interatomic distance is shortened by around 6% in all the six systems. This behavior has also been reported in a previous study [22]. As a result, from a chemical viewpoint, the ternary Zr–Cu–Al system is more stable than the binary Zr–Cu system because the interatomic distance of the Cu–Al pair is shorter.

Finally, the cutoff values for the first shell, i.e., the radial distance corresponding to the first minimum of $g_{ij}(r)$, were obtained from the PRDFs. For example, for the $Zr_{50}Cu_{40}Al_{10}$ system, the cutoff values of Zr–Zr, Zr–Cu, Cu–Cu, Cu–Al, Al–Al, and Al–Zr pairs were 4.15 Å, 3.75 Å, 3.45 Å, 3.45 Å, 3.55 Å, and 3.95 Å, respectively. These values were subsequently used to calculate the CNs and H–A indices in Sections 3.3 and 3.4 respectively.

**Table 1**
Interatomic distances (Å) for $Zr_xCu_{90-x}Al_{10}$ alloys.

| Alloy | $R_{Zr-Zr}$ | $R_{Zr-Cu}$ | $R_{Cu-Cu}$ | $R_{Cu-Al}$ | $R_{Al-Al}$ | $R_{Al-Zr}$ |
|---|---|---|---|---|---|---|
| $Zr_{20}Cu_{70}Al_{10}$ | 3.13 | 2.85 | 2.55 | 2.53 | 2.80 | 3.02 |
| $Zr_{30}Cu_{60}Al_{10}$ | 3.14 | 2.84 | 2.55 | 2.53 | 2.85 | 3.00 |
| $Zr_{40}Cu_{50}Al_{10}$ | 3.16 | 2.84 | 2.53 | 2.55 | 2.83 | 2.96 |
| $Zr_{50}Cu_{40}Al_{10}$ | 3.15 | 2.85 | 2.57 | 2.56 | 2.88 | 2.98 |
| $Zr_{60}Cu_{30}Al_{10}$ | 3.14 | 2.83 | 2.56 | 2.58 | 2.88 | 3.03 |
| $Zr_{70}Cu_{20}Al_{10}$ | 3.15 | 2.86 | 2.56 | 2.57 | 2.82 | 3.04 |

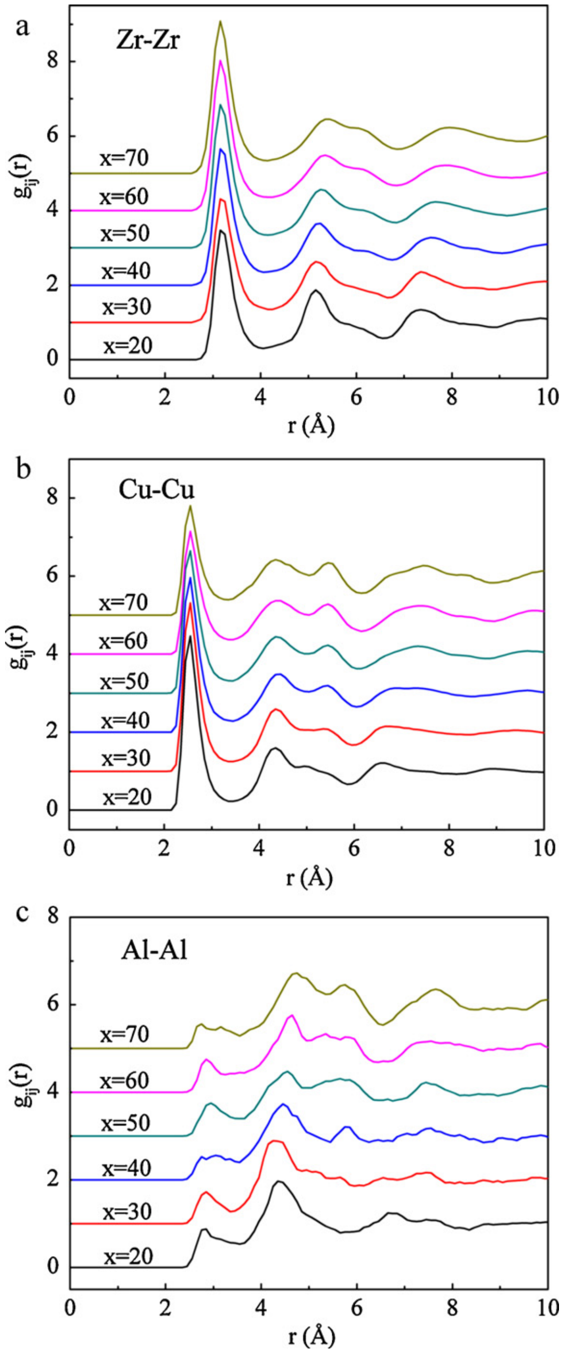

**Fig. 5.** PRDFs for (a) Zr–Zr, (b) Cu–Cu, and (c) Al–Al like bonds for amorphous $Zr_xCu_{90-x}Al_{10}$ alloys. Individual curves corresponding to different alloys are displaced vertically for clarity.

### 3.3. Coordination numbers (CNs)

Table 2 illustrates the total and partial CNs for $Zr_xCu_{90-x}Al_{10}$ alloys. We observe that $CN_{all}$ remains nearly constant at 13 despite changes in composition, and that the CNs for Zr, Cu, and Al decrease with increasing Zr concentrations. $CN_{Zr}$ is the largest of all the six systems, followed by $CN_{Al}$ and then $CN_{Cu}$. This is consistent with the difference in atomic radii ($R_{Zr} = 1.6$ Å, $R_{Al} = 1.43$ Å, $R_{Cu} = 1.28$ Å). Larger atoms possess more neighbor space, which can accommodate more neighbor atoms.

However, the CNs shown in Table 2 are unable to reveal the number of neighbor atoms for each center atom. Fig. 7 shows the distribution of coordination polyhedra for the $Zr_xCu_{90-x}Al_{10}$

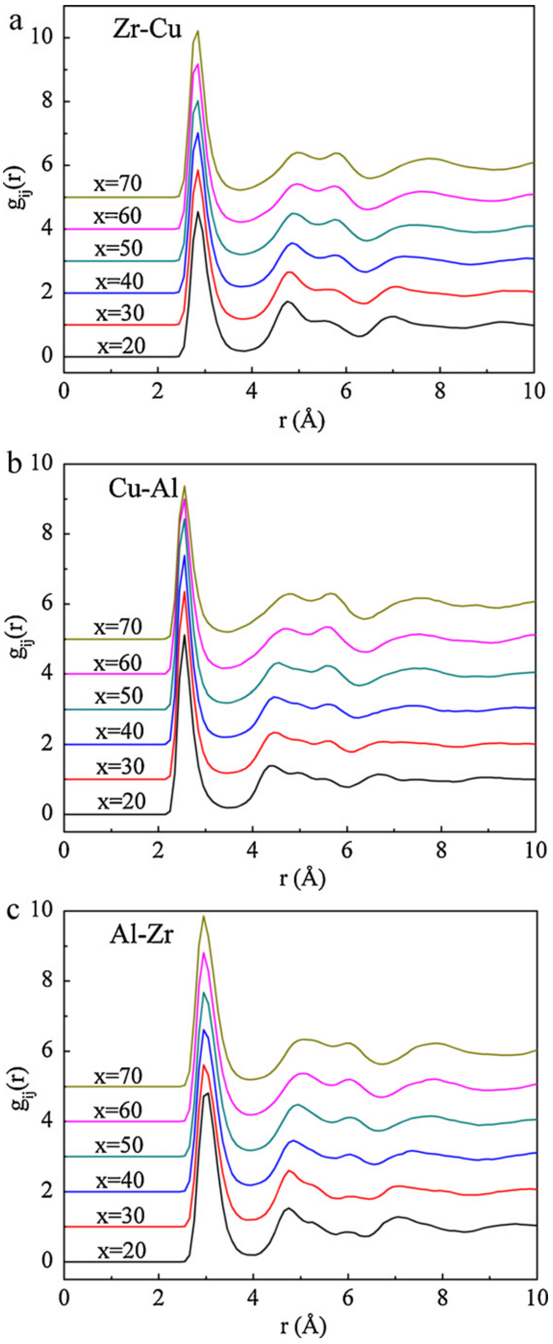

**Fig. 6.** PRDFs for (a) Zr–Cu, (b) Cu–Al, and (c) Al–Zr unlike bonds for amorphous $Zr_xCu_{90-x}Al_{10}$ alloys. Individual curves corresponding to different alloys are displaced vertically for clarity.

**Table 2**
CNs for $Zr_xCu_{90-x}Al_{10}$ alloys.

| Alloy | $CN_{all}$ | $CN_{Zr}$ | $CN_{Cu}$ | $CN_{Al}$ |
|---|---|---|---|---|
| $Zr_{20}Cu_{70}Al_{10}$ | 13.05 | 16.29 | 12.14 | 12.92 |
| $Zr_{30}Cu_{60}Al_{10}$ | 13.06 | 15.84 | 11.73 | 12.66 |
| $Zr_{40}Cu_{50}Al_{10}$ | 13.00 | 15.25 | 11.33 | 12.32 |
| $Zr_{50}Cu_{40}Al_{10}$ | 12.98 | 14.75 | 10.97 | 12.21 |
| $Zr_{60}Cu_{30}Al_{10}$ | 12.95 | 14.25 | 10.68 | 11.98 |
| $Zr_{70}Cu_{20}Al_{10}$ | 12.94 | 13.82 | 10.45 | 11.79 |

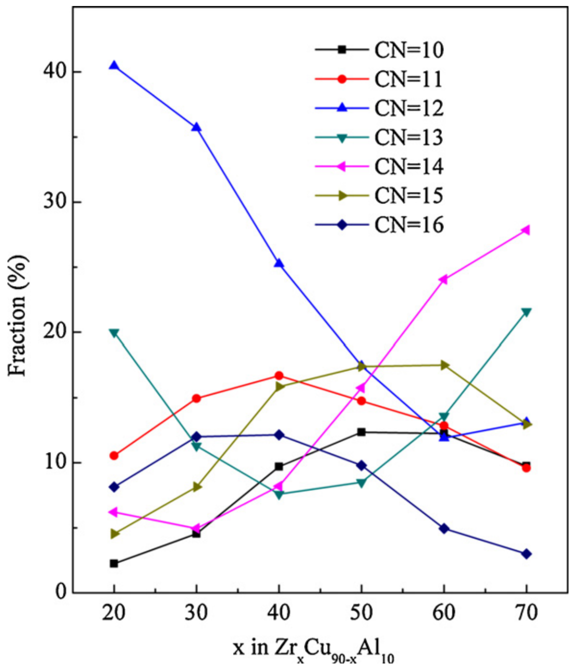

**Fig. 7.** Distribution of coordination polyhedra for $Zr_xCu_{90-x}Al_{10}$ alloys.

alloys. We observe that the fraction of atoms having 12 neighbor atoms decreases from 40% in the $Zr_{20}Cu_{70}Al_{10}$ system to 12% in the $Zr_{70}Cu_{20}Al_{10}$ system. Since one of the prerequisites for an atom to form an icosahedron is that it should possess 12 neighbor atoms, the high fraction of atoms with CN = 12 on the Cu-rich end provides a good foundation for icosahedral formation in these systems.

In addition, we investigated the distribution of CNs for each element. Fig. 8 depicts the major types of coordination polyhedra observed in the $Zr_{50}Cu_{40}Al_{10}$ alloy, which indicates that Cu contributes significantly to the formation of CN = 12, followed by Al, and subsequently Zr, which rarely exhibits CN ≤ 13. However, the fractions shown in Fig. 8 are inadequate for determining the icosahedral-forming ability of each element since Zr and Cu atoms are dominant, while the concentration of Al is quite low. Therefore,

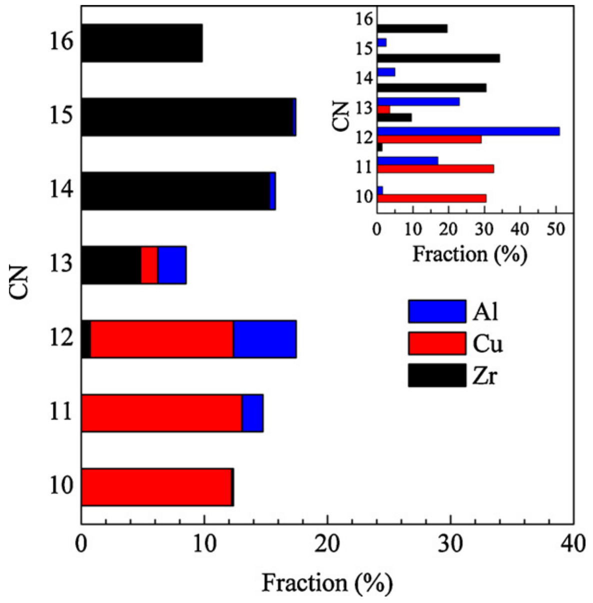

**Fig. 8.** Distribution of coordination polyhedra for $Zr_{50}Cu_{40}Al_{10}$ alloy. The inset illustrates the distribution of coordination polyhedra found in each element.

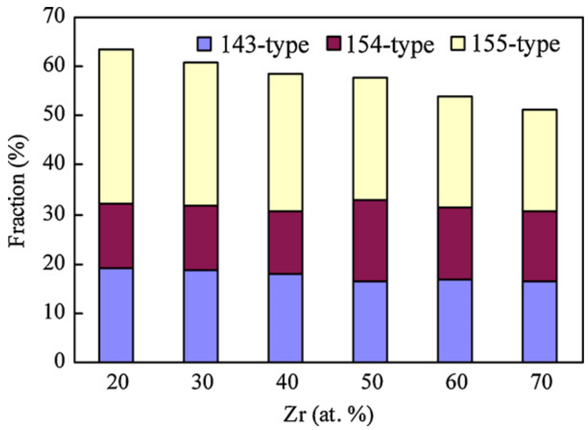

**Fig. 9.** Statistics of H–A indices with icosahedral ordering for amorphous $Zr_xCu_{90-x}Al_{10}$ alloys.

we have also calculated the distribution of coordination polyhedra found in each element (inset of Fig. 8). As shown in the inset, more than 50% of Al atoms have 12 neighbor atoms. In addition, Cu atoms are more likely to form small clusters (with CN ≤ 13); of those, nearly 30% possess 12 neighbor atoms. On the other hand, only a small fraction of Zr atoms possess coordination polyhedra formed by 12 neighbor atoms, while the majority of Zr atoms favor large clusters (with CN ≥ 13). Therefore, these Zr atoms serve as the neighbor atoms of Cu-centered and Al-centered icosahedra. This demonstrates that icosahedral or quasi-icosahedral structures favor smaller atoms as solutes and larger atoms as solvents.

### 3.4. *Common neighbor analysis*

Fig. 9 shows the composition dependence of icosahedral ordering in Zr–Cu–Al MGs. We observe that the fraction of perfect and distorted icosahedral pairs is nearly 65% at the Cu-rich end. However, this value decreases with increasing Zr concentrations. This decrease is mainly due to the reduction in the number of perfect icosahedral pairs, which signifies that atoms are less likely to form full icosahedra at the Zr-rich end.

To gain a greater insight into each individual system, we studied $Zr_{50}Cu_{40}Al_{10}$ as a representative system in more detail in order to determine the distribution of different H–A indices (Fig. 10). It is observed that more than 25% of the system is made up of 155-type pairs, which are contributed mainly by Zr–Cu, Zr–Zr, and Al–Zr bonds. We also find that all icosahedral pairs (i.e., 155-type, 154-type, and 143-type pairs) account for more than 55% of the system, while the crystal pairs (i.e., 166-type, 144-type, and 142-type pairs) are negligible. This again suggests that $Zr_{50}Cu_{40}Al_{10}$ has good icosahedral-forming ability. From the figure, we deduce that unlike pairs are more likely than like pairs to form icosahedral ordering. This is because atomic pairs with large negative heat of mixing ($\Delta H_{mix}$) favor icosahedral formation ($H_{mix}^{Al-Zr} = -44$ kJ/mol, $H_{mix}^{Zr-Cu} = -23$ kJ/mol, $H_{mix}^{Cu-Al} = -1$ kJ/mol).

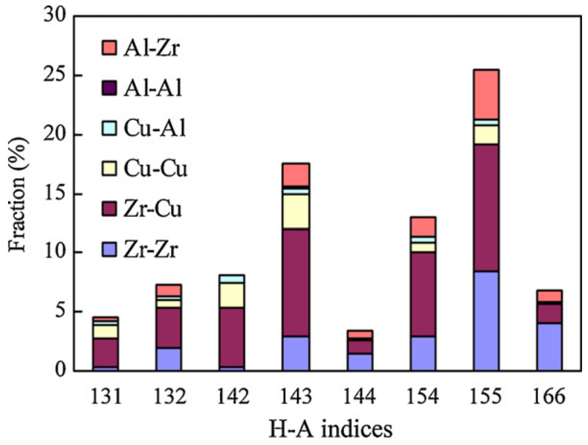

**Fig. 10.** H–A indices distribution for $Zr_{50}Cu_{40}Al_{10}$ alloy.

Our results show that $Zr_{40}Cu_{50}Al_{10}$ and $Zr_{50}Cu_{40}Al_{10}$ have good icosahedral-forming ability, which is in good agreement with previous studies [22,23]. However, we also observe that the addition of Al atoms into the binary Zr–Cu alloy to form a ternary Zr–Cu–Al alloy results in strong icosahedral ordering at the Cu-rich end. The strong interactions of Cu–Al and Al–Zr have disordered the original arrangement of Zr–Cu alloys, which enhances the icosahedral-forming ability. The smaller possibility of forming icosahedral at the Zr-rich end is due to the larger radius of the Zr atom. According to reference [36], the atomic size ratio of the solute to the solvent for an ideal icosahedral structure is about 0.9. If the concentration of Zr is very high, a substantial number of Zr atoms will be surrounded by other Zr atoms, precluding the formation of an icosahedral structure.

## 4. Conclusions

We have studied amorphous Zr–Cu–Al alloys using classical MD simulations. RDF analysis reveals that the interactions of Cu–Al and Al–Zr are quite strong. In particular, the bond length of Cu–Al is shortened by 6% in all six systems studied. Therefore, the original atomic arrangement in Zr–Cu MGs has been perturbed and the icosahedral-forming ability has been enhanced with additional Al atoms. The average CNs of $Zr_xCu_{90-x}Al_{10}$ MGs have also been obtained. The results show that the total CN is almost independent of composition. In addition, by studying the distribution of coordination polyhedra, it is found that Cu atoms are more likely to form smaller clusters, while Zr atoms favor larger clusters. Finally, the distribution of H–A indices suggests that there are more icosahedra when the composition of Cu is larger than that of Zr or when the compositions of Cu and Zr elements are approximately equal in ternary Zr–Cu–Al systems.

## References

[1] W. Klement, R.H. Willens, P. Duwez, Nature 187 (1960) 869–870.
[2] M.H. Cohen, D. Turnbull, Nature 203 (1964), 964–964.
[3] D.B. Miracle, Nature Mater. 3 (2004) 697–702.
[4] H.W. Sheng, W.K. Luo, F.M. Alamgir, J.M. Bai, E. Ma, Nature (London) 439 (2006) 419–425.
[5] Y.Q. Cheng, E. Ma, Prog. Mater. Sci. 56 (2011) 379–473.
[6] Y. Li, Q. Guo, J.A. Kalb, C.V. Thompson, Science 322 (2008) 1816–1819.
[7] N. Mattern, A. Schöps, U. Kühn, J. Acker, O. Khvostikova, J. Eckert, J. Non-Cryst. Solids 354 (2008) 1054–1060.
[8] N. Mattern, P. Jóvári, I. Kaban, S. Gruner, A. Elsner, V. Kokotin, H. Franz, B. Beuneu, J. Eckert, J. Alloys Compd. 485 (2009) 163–169.
[9] N. Mattern, J. Bednarcik, S. Pauly, G. Wang, J. Das, J. Eckert, Acta Mater. 57 (2009) 4133–4139.
[10] J. Antonowicz, A. Pietnoczka, W. Zalewski, R. Bacewicz, M. Stoica, K. Georgarakis, A.R. Yavari, J. Alloys Compd. 509S (2011) S34–S37.
[11] Z.D. Sha, Y.P. Feng, Y. Li, Appl. Phys. Lett. 96 (2010) 061903.
[12] Z.D. Sha, Y.W. Zhang, Y.P. Feng, Y. Li, J. Alloys Compd. 509 (2011) 8319–8322.
[13] G.A. Almyras, C.E. Lekka, N. Mattern, G.A. Evangelakisa, Scripta Mater. 62 (2010) 33–36.
[14] Y. Zhang, N. Mattern, J. Eckert, J. Alloys Compd. 509S (2011) S74–S77.
[15] K.H. Kang, K.W. Park, J.C. Lee, E. Fleury, B.J. Lee, Acta Mater. 59 (2011) 805–811.
[16] P. Yu, H. Bai, M. Tang, W. Wang, J. Non-Cryst. Solids 351 (2005) 1328–1332.
[17] G. Kumar, T. Ohkubo, T. Mukai, K. Hono, Scripta Mater. 57 (2007) 173–176.
[18] Y. Wu, H. Wang, H.H. Wu, Z.Y. Zhang, X.D. Hui, G.L. Chen, D. Ma, X.L. Wang, Z.P. Lu, Acta Mater. 59 (2011) 2928–2936.
[19] P. Yu, K.C. Chan, W. Chen, L. Xia, J. Alloys Compd. 509 (2011) 8518–8521.
[20] Y.Y. Cui, T.L. Wang, J.H. Li, Y. Dai, B.X. Liu, Phys. Chem. Chem. Phys. 13 (2011) 4103–4108.
[21] A. Ishii, A. Iwase, Y. Fukumoto, Y. Yokoyama, T.J. Konno, F. Hori, J. Alloys Compd. 504S (2010) S230–S233.
[22] Y.Q. Cheng, E. Ma, H.W. Sheng, Phys. Rev. Lett. 102 (2009) 245501.

[23] X.D. Wang, Q.K. Jiang, Q.P. Cao, J. Bednarcik, H. Franz, J.Z. Jiang, J. Appl. Phys. 104 (2008) 093519.
[24] J.D. Honeycutt, H.C. Andersen, J. Phys. Chem. 91 (1987) 4950–4963.
[25] H. Jónsson, H.C. Anderson, Phys. Rev. Lett. 60 (1988) 2295–2298.
[26] M. Li, W.L. Johnson, Phys. Rev. Lett. 70 (1993) 1120–1123.
[27] W. Kob, J. Phys. Condes. Matter 11 (1999) R85–R115.
[28] M.S. Daw, M.I. Baskes, Phys. Rev. B 29 (1984) 6443–6453.
[29] F. Cleri, V. Rosato, Phys. Rev. B 48 (1993) 22–33.
[30] S. Melchionna, G. Ciccotti, B.L. Holian, Mol. Phys. 78 (1993) 533–544.
[31] H.J.C. Berendsen, J.P.M. Postma, W.F. van Gunsteren, A. DiNola, J.R. Haak, J. Chem. Phys. 81 (1984) 3684–3690.
[32] J.M. Haile, Molecular Dynamics Simulation: Elementary Methods, John Wiley & Sons, Inc, New York, 1992.
[33] H. Tsuzuki, P.S. Branicio, J.P. Rino, Comput. Phys. Commun. 177 (2007) 518–523.
[34] A.S. Clarke, H. Jónsson, Phys. Rev. E 47 (1993) 3975–3984.
[35] H. Nagai, M. Mamiya, T. Okutani, J. Non-Cryst. Solids 357 (2011) 126–131.
[36] D.R. Nelson, F. Spaepen, Solid State Phys. 42 (1989) 1–90.